Understanding the impact of Fc glycosylation on its conformational changes by Molecular Dynamics Simulations and Bioinformatics

Journal:	*Molecular BioSystems*
Manuscript ID	MB-ART-09-2015-000602.R2
Article Type:	Paper
Date Submitted by the Author:	13-Oct-2015
Complete List of Authors:	Zhang, Yubo; Biological New Drug Research Institute, Innovative Pharmaceuticals,

Molecular Biosystems

PAPER

Understanding the impact of Fc glycosylation on its conformational changes by Molecular Dynamics Simulations and Bioinformatics

Yubo Zhang,*[a]

N-linked glycosylation of Fc at N297 plays an important role in its effector function, aberrance of which would cause disease pathogenesis. Here, we performed all-atom molecular dynamics simulations to explore effects of Fc glycosylation on its dynamics behaviors. Firstly, equilibrium simulations suggested Fc deglycosylation was able to induce residual flexibility in its CH2 domain. Besides, free energy landscape revealed three minimum energy wells in deglycosylated Fc, representing its "open", "semi-closed" and "closed" states. However, we could only observe the "open" state of glycosylated Fc. Supportively, principal component analysis emphasized the prominent motion of delyclosylated Fc and dynamically depicted how it changed from the "open" state to its "closed" state. Secondly, we studied the recognition mechanism of the Fc binding to its partners. Energy decomposition analysis identified key residues of Fc to recognize its two partners P13 and P34. Evidently, electrostatic potentials surfaces showed electrostatic attraction helped to stabilize the interaction between Fc and its partners. Also, relative binding free energies explained different binding affinity in Fc-P13 and Fc-P34. Collectively, these results together provided structure basis for understanding conformational changes of deglycosylated Fc and the recognition mechanism of the Fc binding to its partners.

Introduction

Immunoglobulins (Igs), consisting of two heavy and two light chains, are the major secretory products of the adaptive immune system[1]. Human Igs are composed of five classes, namely IgM, IgG, IgA, IgE, and IgD. Among them, IgG constitutes over 75% of Igs, which is the most abundant Ig in serum[2, 3]. Fc is the crystalizable fragment of Igs, function in mediating complement-dependent cytotoxicity (CDC) and antibody-dependent cell cytotoxicity (ADCC)[1].

The CH2 domain of Fc contains a conserved N-linked glycosylation site (N297),which helps Fc maintain its quaternary structure and stability[4, 5]. Importantly, aberrant glycosylation of Fc is closely associated with disease pathogenesis. For instance, low-galactose-containing IgG glycoforms were found in many diseases such as Rheumatoid Arthritis (RA), juvenile chronic arthritis (JCA), tuberculosis, and active Crohn's disease[1, 6]. Particularly in RA[1], the level of agalactosyl glycoforms of IgG (IgG-G0) significantly increased in comparison with that of healthy controls. Remission of the disease would decrease levels of IgG-G0. Hence, investigating the molecular mechanism of Fc glycosylation would help us to understand its impacts on pathogenesis.

Given the importance of Fc glycosylation, different approaches were previously used to explore its molecular mechanism. Pioneering X-ray crystallography determined static structures of fully glycosylation of Fc and truncated glycoforms of Fc[7]. The "open" conformation was observed in glycosylated Fc, while the "closed" conformation was found in truncated glycoforms of Fc. In addition, Differential Scanning Calorimetry (DSC) [8] was used to evaluate thermal stability of Fc in its different glycoforms. Besides, Fourier Transform Infrared spectroscopy and Intrinsic Fluorescence spectroscopy[8] were used to study secondary and tertiary structure of deglycosylated and glycosylated Fc. Results from these experiments together depicted the property of Fc glycosylation. However, there are still some questions need to be answered: What is the dynamic behaviors of deglycosylated Fc? How can Fc transit from its "open" conformation to the "closed" conformation?

Currently, the *in silico* studies are good complementary to experimental approaches. Specially, all-atomic molecular dynamics (MD) simulations can directly reflect protein dynamic behaviors and was widely used in exploring protein conformational change[9-12]. Free Energy Landscape was used to investigate different intermediate states of proteins by mapping their energy distribution[12]. Additionally, Principal Component Analysis (PCA) was also used to study transition mechanism between different protein conformations[13].

[a] *Biological New Drug Research Institute, Innovative Pharmaceuticals, Guangdong*
**corresponding author. Dr. Yubo Zhang Email: zhyubo7@gmail.com*

In this work, we employed MD simulations to explore impacts of Fc glycosylation on its conformational changes. Firstly, free energy landscape identified three states of Fc when it was deglycosylated. Besides, principal component analysis investigated conformational changes of deglycosylated Fc. Secondly, relative binding free energies were calculated to identify key residues responsible for the Fc binding to P13 and P34. In addition, analysis from electrostatic potentials suggested electrostatic attractions played a key role in maintaining the binding affinity between Fc and its partners. Collectively, our results can provide structural basis to understand dynamic behaviors of Fc induced by its deglycosylation, and may be helpful for exploring the recognition mechanism between Fc and its partners.

Materials and methods

Atomic Coordinates

Crystal structures of Fc-P13 and Fc-P34 were obtained directly from the Protein Data Bank, the PDB IDs of which were 1dn2[14] and 1l6x[15]. These two complexes were called Fc-P13 and Fc-P34 because two partners of Fc were a 13-aa peptide and a 34-aa peptide. Fc-P13 was used as the template structure for the construction of deglycosylated Fc by removing its glcans. For structure refinement, complexes were then subject to energy minimization in GROMACS 4.5.3 program [16], aiming to relieve side chain steric clashes and overlaps.

MD simulation with Explicit Solvent

The MD simulations were performed with the GROMACS 4.5.3 software package [16] using the ff99 force field[17, 18] and the TIP3P water model as our previous reports[10, 12]. Glycans were defined using generalized amber force field (GAFF) parameters[19] and AM1-BCC partial charges were added using ANTECHAMBER[20] followed by conversion to GROMACS compatible topology using ACPYPE[21]. The protonation state of ionizable groups was chosen to correspond to pH 7.0. Counter ions were added to compensate the net charge of the system. The initial structure of the complex was immersed in a periodic water box. The electrostatic interactions were calculated by using the Particle-mesh Ewald (PME) algorithm [22], and the van der Waals forces were treated with a cutoff distance of 10 Å. After 3000 steps of energy minimization using a steepest descent method, the system was subject to equilibration at 300 K and normal pressure, using harmonic position restraints with a force constant of 1000 kJ mol^{-1} nm^{-2}. The system was coupled to an external bath by the Berendsen pressure and temperature coupling method [23]. The production run was performed under the same conditions except that all position restraints were removed. The results were analyzed using the standard software tools provided by the GROMACS package [16]. The in-house analysis scripts and protocols were performed as our previous literatures[9-12]. Visualization and manipulation of the structures was performed using the programs visual molecular dynamics (VMD) [24] and Swiss-PdbViewer 3.7 [25].

Thermodynamic Calculation

The binding free energy for the Fc binding to its partners P13 and P34 was calculated by the MM-GBSA approach [26-32].

In this study, the implicit generalized Born solvation model was used (igb=2) [33], with dielectric constants for solute and solvent set to 1 and 80[34]. The temperature was set to 300 K. Non-bonded interactions were cut off at a distance of 12 Å. The ff99 force field (Parm99) [18] was applied throughout the energy minimization and MD simulations.

In the MM-GBSA implementation of Amber 11.0[35], the binding free energy of A+B→AB is calculated using the following thermodynamic cycle:

$$A_{aqu} + B_{aqu} \xrightarrow{\Delta G_{binding}} AB_{aqu}$$

$$A_{gas} + B_{gas} \xrightarrow{\Delta G_{gas}} AB_{gas}$$

$$\Delta G_{binding} = \Delta G_{gas} - \Delta G^{A}_{solv} - \Delta G^{B}_{solv} + \Delta G^{AB}_{solv}$$

$$= \Delta H_{gas} - T\Delta S - \Delta G^{A}_{GBSA} - \Delta G^{B}_{GBSA} + \Delta G^{AB}_{GBSA}$$
$$= \Delta H_{gas} - T\Delta S + \Delta\Delta G_{GB} + \Delta G_{SA}$$

$$\Delta H_{gas} \approx \Delta E_{gas} = \Delta E_{intra} + \Delta E_{elec} + \Delta E_{vdw}$$

$$\Delta\Delta G_{GB} = \Delta G^{AB}_{GB} - \left(\Delta G^{A}_{GB} + \Delta G^{B}_{GB}\right)$$

$$\Delta\Delta G_{SA} = \Delta G^{AB}_{SA} - \left(\Delta G^{A}_{SA} + \Delta G^{B}_{SA}\right)$$

Where T is the temperature, S is the solute entropy, ΔG_{gas} is the interaction energy between A and B in the gas phase, and ΔG^{A}_{solv}, ΔG^{B}_{solv}, and ΔG^{AB}_{solv} are the solvation free energies of A, B, and AB, which are estimated using a GB surface area (GBSA) method [26, 27]. That is, $\Delta G^{AB}_{solv} = \Delta G^{AB}_{GBSA} + \Delta G^{AB}_{GB} + \Delta G^{AB}_{SA}$, and so forth. ΔG_{GB} and ΔG_{SA} are the electrostatic and nonpolar terms, respectively. The bond, angle, and torsion energies constitute the intramolecular energy ΔE_{intra} of the complex, while ΔE_{elec} and ΔE_{vdw} represent the receptor-ligand electrostatic and van der Waals interactions, respectively. Because of the constant contribution of $-T\Delta S$ for each complex, we refer to $\Delta G^{*}_{binding}$ for $\Delta G_{binding} + T\Delta S$ in the discussion. To verify the quality and validity of the resulting complexes, the relative binding free energy $\Delta G^{*}_{binding}$ was calculated by using MM-GBSA for post processing snapshots from the MD trajectories. Previous MM-GBSA studies[36-38] showed 30, 40 and 100 snapshots could give reasonable results in correlation with experimental data. Here, we collected 50 and 250 snapshots at the final equilibrium stage for calculation, both of which exhibited similar results (Table 1 and Table S1).

Free energy landscape

The free energy landscape of the dynamic behaviors of Fc was estimated by an appropriate sampling method. In order to get a two dimensional energy landscape map, RMSD and Rg of Fc were chosen as two reaction coordinates. The energy landscape was calculated along these two reaction coordinates as equation shown[12, 13]:

$$\Delta G(p1, p2) = -k_B T \, ln\rho(p1, p2)$$

Where k_B represented the Boltzmann constant, T was the simulated temperature, and $\rho(p1, p2)$ represented the normalized joint probability distribution.

Principal component analysis

The principal component analysis (PCA) was applied to highlight the correlation differences between glycosylated and deglycosylated Fc. This method was based on the diagonalisation of the covariance matrix, which was built from the atomic fluctuations after the removal of the translational and rotational movement. The covariance matrix between the Cα atoms *i* and *j* of Fc, were defined as:

$$C_{ij} = \langle (x_i - \langle x_i \rangle)\big(x_j - \langle x_j \rangle\big)\rangle \; (i, j = 1,2,3,\ldots,3N)$$

where x_i and x_j are Cartesian coordinates of the *i*th and *j*th Cα atom, N is the number of the Cα atoms considered, and $\langle x_i \rangle$ and $\langle x_j \rangle$ represent the time average over all the configurations obtained in molecular dynamics simulation[39].

Electrostatic potentials surfaces

Electrostatic potential maps were calculated with the Adaptive Poisson-Boltzmann Solver (APBS) [40] according to default parameters (physiological salt concentration of 150 mM, temperature of 298.15 K, solvent dielectric of 78.00, and solute dielectric of 2). Solute charges were distributed onto grid points using a cubic B-spline discretization. The molecular surface was defined by the interface between the radius of a water molecule (1.4 Å), and the solute van der Walls radii.

Results

Stability of Simulation Systems

To explore how Fc glycosylation affects its structural stability, we constructed two simulation systems, in which the Fc proteins were glycosylated and deglycosylated.
First, we monitored root-mean-square deviation (RMSD) of these two proteins during MD simulations, reflecting the stability of protein structures. We calculated the RMSD values of the Fc domain with respect to its initial structure before the production simulation. Fig. 1 showed glycosylated Fc had the RMSD values of ~2Å, suggesting this system maintained its equilibrium state along 50ns MD simulation. Similarly, the RMSD values of its backbone also confirmed the stability of the simulation system. Afterwards, we focused on the RMSD values of deglycosylated Fc. Fig. 1 showed the RMSD values of deglycosylated Fc jumped to ~3.5Å at 10ns. Significantly, this value increased to ~5Å at 20ns and then maintained to 3.5Å till the end of the simulation. Trajectories from these two simulations can be inspected in Movie 1 and Movie 2. Evidently, this suggested Fc deglycosylation was able to induce obvious residual fluctuation during simulation.

In Fig. S1, we extended 20ns MD simulations for both of these two systems and evaluated the stability of these systems between 50ns and 70ns. In glycosylated Fc, the RMSD values maintained around 1.5~2Å. After extraction two snapshots at 50ns and 70ns, we superimposed them with the X-ray structure. The structural similarity of these structures suggested the system could reach its equilibrium state. As to deglycosylated Fc, we observed the RMSD values fluctuated around 3.8 Å between 50 and 70ns. Additionally, two snapshots extracting at 50 and 70ns exhibited residual fluctuation with respect to the X-ray structure. Altogether, the pattern of residual fluctuation for deglycosylated Fc between 50 and 70ns was similar with that between 0ns and 50ns.

To further understand if residual fluctuation was related to its secondary structure, we calculated the integrity of the secondary structure of glycosylated and deglycosylated Fc. Fig. 1 showed secondary structure of deglycosylated Fc was similar with that of glycosylated Fc. This suggested stability and integrity of secondary structure in these two systems.

Structural flexibility

To investigate structural flexibility of deglycosylated Fc and glycosylated Fc during simulations, we measured Cα RMSF with respect to its initial structure throughout the trajectory. Expectantly, Fig. 2 showed significant structural flexibility in deglycosylated Fc, while in the absence of glycosylated Fc. In deglycosylated Fc, residues from 237 to 349 had the significant fluctuation and their RMSF values were around 3 Å. However, in glycosylated Fc, the RMSF values of these residues were ~1.5Å. These emphasized deglycosylation of Fc were able to induce significant residue flexibility from 237 to 349. Take a closer to this region (shown in the Fig. 2), we noticed most of these residues distributed in the CH2 region of Fc. Specially, they can form and stabilize a glycans-filled cavity in glycosylated Fc. However in deglycosylated Fc, due to the absence of these glycans, residues forming the central cavity were significantly flexible, contributing to induce structural flexibility of Fc.

Free energy landscape

To explore dynamic behaviors of Fc in its deglycosylated and glycosylated states, we constructed the free energy landscape to reflect protein conformational changes. We defined two reaction coordinates of free energy landscape: one was RMSD of Fc, exhibiting protein structural stability during the MD simulations; the other was radius of gyrate (Rg) of Fc, reflecting whether Fc was stably folded.
Fig. 3A showed three major deep wells in the free energy landscape when Fc was in its deglycosylated state. These three

wells were positioned at the coordinates (3.5 Å, 26.0 Å), (4.0 Å, 25.4 Å), and (5.0 Å, 25.0 Å). Extraction of snapshots from these three wells (Fig. 3A) suggested significant conformational changes of deglycosylated Fc. Notably, three snapshots (A, B and C) represented “open”, “semi-open” and “closed” states. The populations of the "open", "semi-open" and "closed" conformers were 35.56%, 55.68% and 8.64% approximately. In snapshot A, two monomers opened their “arms” and were able to form a cavity. The size of this cavity was reduced in the “semi-open” state according to snapshot B. In addition, the cavity of snapshot C was in its “closed” state and arms of two monomers packed together. The free energy landscape suggested these three distinguish conformations were probably able to transform to each other smoothly by their crossing the low energy barrier. We also provided time scale for the motion of dominant (shown in Fig. S2). After an extraction of time ranging from 10.8 to 18.7ns, we observed a cycle containing the “open” (10.8ns), “closed” (13.8ns), and “open” (18.7ns) states.

Fig. 3B described the free energy landscape when Fc was glycosylated. There was only one major well centered at the coordinate (1.8 Å, 26.7 Å), exhibiting its lowest energy value. The structure of this well adopted an open conformation, in which two monomers opened their arms to form a visible cavity. This “open” state of glycosylated Fc stabilized along the whole simulation.

Distance analysis

Importantly, we need to get an insight into atomic detailing of Fc in its glycosylated and deglycosylated states. To this end, we focused on five residues G237, P238, S239, V240, F241, locating in the CH2 region of two Fc monomers. Note that these residues were able to form five residue pairs: G237-G237, P238-P238, S239-S239, V240-V240 and F241-F241 (Fig. 4A), positioning two sides of the glycans-filled cavity. Fig. 4B showed the distances between the Cα atoms of these residue pairs during simulations. Visibly, the distance of G237-G237 in glycosylated Fc was around 20Å (colored in black), while it reduced to ~10 Å (colored in green) in deglycosylated Fc. Similarly, the distances of P238-P238 and S239-S239 in glycosylated Fc was around 25 Å (colored in black-red), and it changed to 15 Å (colored in black-green) in deglycosylated Fc. Distances of V240-V240 and F241-F241 also decreased approximately from 30 Å (colored in red) to 23 Å (colored in black-red) when Fc was deglycosylated. Collectively, Fc deglycosylation was able to shorten distances between these residues in the CH2 region, disrupting the glycans-filled cavity.

Principal component analysis

To explore how Fc deglycosylation induced its conformational change, we adopted principal component analysis (PCA) to detect the most prominent motion of Fc. In the porcupine plots (Fig. 5), each C-alpha has a cone, pointing to the direction of the atom motion. The size and length of cones represent the number of Cα atoms and the amplitude of the atoms motion, respectively. First, deglycosylated Fc has more and larger cones than glycosylated Fc, distributing around the CH2 region of Fc. Evidently, this suggested Fc deglycosylation was able to induce conformational change of the CH2 domain. Second, the direction of these cones was moving towards the glycans-filled cavity. Movie 3 and Movie 4 showed motions of glycosylated and deglycosylated Fc along the first eigenvector. In addition, we extracted the first and last snapshots from the first principal component (PC1) of deglycosylated Fc. Observably, these two snapshots represented “open” and “closed” states. However, there was merely one snapshot representing the “open” state in glycosylated Fc. Supportively, different conformations observed from PCA were consistent with those from previous free energy landscape. Analysis of the porcupine plots emphasized the prominent motion of delyclosylated Fc and gave a reasonable explanation to how its conformation changed from the “open” state to the “close” state.

Energy decomposition analysis

The characteristic of the Fc binding to its receptor FcRn was widely used to develop new biological drugs in recent years. The binding region of Fc located around its two flanks, consisting of two α-helices and non-structural coils. Fig. 6A and 6C highlighted this binding region by superimposing of Fc (colored in red) in complex with P13 (colored in blue), P34 (colored in yellow) and FcRn (colored in green). Apparently, these three complexes shared similar Fc binding domain, positioning around the flanks of Fc. This arises one interesting question: What is atomic detailing as Fc binds its partners? To answer this question, we decomposed binding free energies into each residue on Fc. In the Fc-P13 complex, we found the binding free energies of M252 and I253 on Fc were -1.64 and -1.55 kcal/mol. As to P13, the binding partner of Fc, three residues L9, V10 and W11 contributed -0.59, -1.79, and -0.88 kcal/mol to free energies.

In addition, we analyzed energy decomposition of residues in the Fc-P34 complex. Fig. 6B exhibited the essential residues on Fc contributing to the binding affinity included L251, M252, I253, S254, T256, L309, H433, N434 and H435. Their binding energies were -1.39, -2.12, -9.21, -1.28, -3.15, -1.39, -1.05, -2.7 and -1.36 kcal/mol. It should also be noted that two residues M252 and I253 were identified as binding residues in the Fc-P13 complex, emphasizing Fc may adopt a general mechanism to recognize different partners. Also, we identified seven residues on P34 for the Fc binding, which were Q11, R12, F14, Y15, L18, I32 and R36. They contributed -4.86, -1.28, -3.81, -5, -1.55, -1.01 and -4.14 kcal/mol for the binding energies.

Electrostatic Potentials Surfaces

The Electrostatic Potential Surfaces (EPS) of Fc was claculated with Linearized Poisson-Boltzmann Equation (LPBE) mode in the APBS package. This method solves a molecule using an algorithm of single DH sphere boundary condition and generates a 3D surface skin model colored by electrostatic

potential. Dielectric constants for protein and solvent were 2.0 and 78.0 in the calculations. Fig. 7 showed there were three regions A, B and C on the interface of Fc. Notably, Region B was embraced by two regions A and C, electrostatic potentials of which were negative. We noticed region A had a tendency to form a negative pocket, interacting directly with residues from peptides P13 and P34. Similarly, region C was electronegative, which was partially divided by electropositive region. This region was able to recognize residues from P34. In addition, we found region B had some residues such as M252 and S254 (Fig. 8), function in increasing FcRn-IgG binding affinity and extending serum half-life. Collectively, these observations showed the charge distribution on the surface of Fc played important roles for recognizing residues from its binding partners, and the proper interactions between Fc and its partners were initiated by electrostatic forces.

Binding free energy

To quantitative estimate binding affinity of Fc in complex with P13 and P34, we performed MM-GBSA to calculate binding free energies and their components between ligand and receptor. Table 1 and Table S1 described relative binding free energies for Fc with P13 and P34, which were calculated from 50 and 250 snapshots at the final equilibrium stage. Additionally, we calculated different components of the binding free energies. We found both electrostatic energy and van der Waals energy in gas phase contributed significantly to the binding free energy. Particularly, the electrostatic energy can provide more favorable contribution for the Fc binding to P13 and P34. Table 1 also showed the electrostatic energy between Fc and P13 was -293.33 kcal/mol, which is stronger than that between Fc and P34.

Further, we calculated contribution of solvation energy for the Fc binding to its partners. Obviously, the nonpolar solvation energy is favorable for the Fc binding to ligands, while the polar solvation energy is unfavorable. Specially, the polar solvation energy of Fc-P13 was 306.76 kcal/mol, exhibiting the most unfavorable energy contribution. This also indicated the water molecules may not play key role in bridge during the Fc recognition.

Discussion

Given the importance of Fc glycosylation, both *in-vitro* and *in-silico* methods were used in previous studies to explore effects of glycans on Fc. Previous MD simulations[41] suggested both deglycosylation and thermal stress affected protein stability of a full length murine IgG2. Accordingly, the Cα RMSD values of glycosylated Fc were 2.5-3.8 Å, while it stabilized at ~2 Å in the current work. It should be noted that this study focused on Fc, while not including the Fab region. In absence of glycans, the Cα RMSD values were ~3.3-4.1 Å for Fc of murine IgG2 while they were 3.5~5 Å in our system, indicating Fc deglycosylation does significantly affect protein stability in our and previous systems.

Spectroscopic experiments[8] were performed to assess the structural integrity of Fc after its deglycosylation. FTIR analysis exhibited the overlay of second derivative spectra between glycosylated and deglycosylated Fc, suggesting no dramatic secondary structural differences in these samples. In addition, intrinsic fluorescence spectroscopy showed these two samples have similar emission peak patterns, indicating no significant differences in their tertiary structures. Expectantly, our *in-silico* results suggested deglycosylated Fc was able to maintain its structural integrity during 50ns MD simulations, correlating well with previous spectroscopic data.

Pioneering X-ray crystallography determined structures of homogeneous, truncated glycoforms of IgG-Fc[7], providing us invaluable information to observe Fc in its different conformations. The superposition of these Fc structures suggested truncation of sugars enable the CH2 domains to approach each other by tilting around the CH2-CH3 joint. Additionally, the CH3 domains were rigid enough to maintain their original position. This emphasized the structural flexibility of the CH2 domain when Fc was deglycosylated. Indeed, B-factor analysis also suggested shorter glycans had higher B-factor, indicating a higher level of flexiblity of Fc[7]. This was also proved by the DSC experiment[8]. Thermal stability evaluation by DSC suggested the transition temperature of the CH2 domain in deglycosylation Fc was 6-8℃ lower in comparison with that in glycosylated Fc. This supported the presence of glycans was able to stabilize the CH2 domain in the process of temperature-induced unfolding. In our simulations, we observed three distinct states of Fc in absence of its glcans, representing “open”, ”semi-open”, and ”closed” conformations. We exhibited the possibility of their transition by analyzing free energy landscape. This was confirmed by subsequent distance analysis on five residues G237, P238, S239, V240 and F241, locating in the CH2 region of two Fc monomers. Additionally, the first principle component on deglycosylated Fc depicted how the “open” state of Fc tranformted to its “closed” state. Collectively, results from simulations supported previous crystallography data[7] and spectrophy data[8], which enable us to understand how Fc deglycosylation induced its conformational change.

After superposition of Fc in complex with its different partners, we found the partners were able to recognize Fc in an overlapping region. Significantly, we identified several key residues on Fc, accounting for its binding to FcRn (Fig. 8). Firstly, three residues M252, S254 and T256 contributed -2.12, -1.28 and -3.15 kcal/mol to the binding free energies. Supportively, *in-vitro* studies suggested IgG with M252Y/S254T/T256E mutations resulted in a 10-fold increase in their binding to FcRn and *in-vivo* experiments showed a 4-fold increase in serum half-life[42, 43]. Secondly, free energy analysis also suggested the residue N434 contributed -2.7 kcal/mol to the free energy. Similarly, previous *in-vitro* experiments exhibited two mutants N434A and N434W resulted in 4- and 80-fold increased binding to FcRn[43, 44]. Also, the *in-vivo* experiment suggested these two mutants were able to increase 1.6- and 2.3-fold in serum half-life[43, 44]. Collectively, our *in-silico* results were in good agreement with previous in-vitro and in-vivo data.

The biological implication of this work is to provide structural and dynamical basis for Fc engineering. Given that Fc glycosylation is closely associated with disease pathogenesis, different engineering approaches were used to optimize the most efficient glycoforms[6]. Generally, selection of cell lines and modification of culture conditions would be helpful to produce IgG in different

glycans[45]. For instance, Croset *et al* [46] expressed 12 proteins in two different cell lines HEK and CHO. Significantly, the proteins exhibited different migration on SDS-PAGE and IEF. Similarly, they showed different mass peak distributions on mass spectrometry and different glycostructures in CGE. In this study, we also observed significant conformational changes induced by Fc deglycosylation. Hence, the *in-silico* approach provided the possibility to large-scale screen the appropriate glycoforms for Fc.

Figure legand

Figure 1: (A) RMSD of glycosylated and deglycosylated Fc with respect to the starting structures for all-atoms (blue), and for Cα (red) during the 50 ns production simulations. (B) Time evolution of secondary structure elements in glycosylated and deglycosylated Fc. The α-helices and β-sheets are shown in red and yellow. The number of residues is labelled at the Y-axis.

Figure 2: (A) RMSF of Cα for deglycosylated (blue) and glycosylated (red) Fc over the simulation. (B) A close view of Fc in its glycosylated state. Glycans are in vdW representations (shown in yellow) yellow and the CH2 regions are in surface representations (Chain A shown in blue and chain B shown in red).

Figure 3: The two-dimensional free energy landscape as a function of Rg and RMSD (defined in the text) for (A)deglycosylated and (B) deglycosylated Fc along 50ns MD simulations. Snapshots from minimum energy wells were extracted.

Figure 4: (A) Residues arranged on two sides of the glycans-filling gravity. (B) The Cα distances of residue pairs G237-G237, P238-P238, S239-S239, V240-V240 and F241-F241 of Fc in its glycosylated and deglycosylated states during simulations.

Figure 5: Dominant motions ensemble using Principal Component Analysis. Porcupine plots of the first eigenvector in (A) deglycosylated Fc and, (B) glycosylated Fc. The first and last snapshots in the first eigenvector were extracted.

Figure 6: (A) Residues on Fc responsible for its binding to P13 and P34. (B) Per-residue interaction spectrum of the residues of Fc with P13 and P34 according to MM-GBSA free energy decomposition analysis. (C) Superimposition of three protein complexes Fc-P13 (PDB id: 1dn2), Fc-P34 (PDB id: 1l6x) and Fc-FcRn (PDB id: 1FRT).

Figure 7: Skin representation of the EPS of Fc extracted from the X-ray structures. Red: ESP < −5 kT/e, blue: >+5 kcal/e, grey: between −5 and +5 kT/e. Residues on P13 (PDB id: 1dn2) and P34 (PDB id: 1l6x) responsible for the binding of Fc are in stick representations (shown in green). P13 and P34 are in cartoon representations (shown in yellow).

Figure 8: A close view of interactions in the Fc-P13 and Fc-P34 complexes. Residues M252, S254, M428 and N434, which were essential to interact with residues on P13 and P34 by previous in-vitro and in-vivo studies, were in surface representations (shown in blue). Recognition residues on P13 (PDB id: 1dn2) and P34 (PDB id: 1l6x) are in stick representations (shown in green). Fc is in a surface representation (shown in red).

Electronic Supplementary Information (ESI) available:

Movie Description

Movies 1 and 2 represent the whole 50ns trajectory of glycosylated Fc (Movie 1, shown in red) and deglycosylated Fc (Movie 2, shown in blue). The X-ray structure is used as a reference (shown in gray). Movies 3 and 4 represent motions of glycosylated Fc (Movie 3) and deglycosylated Fc (Movie 4) along the first eigenvector.

Supplemental_material

Figure S1: RMSDs of glycosylated and deglycosylated Fc with respect to the starting structures for all-atoms (blue), and for Cα (red) during the 70 ns production simulations. Superimposition of one X-ray structure and two snapshots extracted at 50ns and 70ns.

Figure S2: Time scale between 10.8ns and 18.7ns is extracted. Three snapshots representing open (10.8ns), closed (13.8ns) and open (18.7ns) states are in surface representations.

Table S1: The free energies calculated by the MM-GBSA methods

Table 1. The free energies calculated by the MM-GBSA methods for the binding of Fc to its partners P13 (PDB id: 1nd2) and P34 (PDB id: 1l6x).

Contribution[a]	1dn2	1l6x
ΔE_{ele}	-293.33±21.67	-191.84±15.13
ΔE_{vdW}	-103.45±5.61	-122.93±5.71
ΔE_{gas}[b]	-396.78±21.77	-314.78±17.21
ΔG_{GB}	323.60±19.39	237.84±14.01
$\Delta G_{sol\text{-}np,GB}$	-16.85±0.41	-19.58±0.64
$\Delta G_{sol,GB}$[c]	306.76±19.33	218.26±13.71
$\Delta G_{ele,GB}$[d]	30.27±5.25	46.00±5.58
$\Delta G_{bind,GB}$[e]	-90.03±6.48	-96.52±6.60

[a] All energies are in kcal/mol.

[b] $\Delta E_{gas} = \Delta E_{ele} + \Delta E_{vdW}$

[c] $\Delta G_{sol,GB} = \Delta G_{sol\text{-}np,GB} + \Delta G_{GB}$

[d] $\Delta G_{ele\text{-}GB} = \Delta G_{GB} + \Delta E_{ele}$

[e] $\Delta G_{bind,GB} = \Delta E_{ele} + \Delta E_{vdW} + \Delta G_{sol,GB}$

Conclusions

It is generally accepted that aberrant glycosylation of Fc is closely associated with disease pathogenesis. However, the dynamic behaviors of deglycosylated Fc are still not fully understood. This work aims to explore the conformational changes of Fc in its deglycosylated state. Observably, there are three minimum energy basins in the free energy landscape of deglycosylated Fc, representing “open”, “semi-closed” and “closed” states. Supportively, principal component analysis dynamically depicts how the “open” state changes to the “closed” state.

On the other hand, we investigate the binding mechanism of Fc to its partners, which plays important roles in developing biological drugs. To this end, we decompose energies into per residue components and identify key residues of Fc to recognize its two partners P13 and P34. Importantly, we notice electrostatic attraction helps to stabilize these two complexes. Besides, calculation of relative binding free energy explains different binding affinity in Fc-P13 and Fc-P34. Collectively, this work will provide *in-silico* evidence to understand the conformational changes of deglycosylated Fc and the recognition mechanism for the Fc binding to the partners.

Acknowledgements

The author thanks Prof. Yi Ding for his insightful comments on the manuscript. Additionally, he thanks David Case for his kindly granting an academic licence for the Amber 11 program.

References

1. J. N. Arnold, M. R. Wormald, R. B. Sim, P. M. Rudd and R. A. Dwek, *Annu Rev Immunol*, 2007, **25**, 21-50.
2. J. Deisenhofer, *Biochemistry*, 1981, **20**, 2361-2370.
3. R. A. Dwek, *Biochem Soc Trans*, 1995, **23**, 1-25.
4. Y. Mimura, S. Church, R. Ghirlando, P. R. Ashton, S. Dong, M. Goodall, J. Lund and R. Jefferis, *Mol Immunol*, 2000, **37**, 697-706.
5. Y. Mimura, P. Sondermann, R. Ghirlando, J. Lund, S. P. Young, M. Goodall and R. Jefferis, *J Biol Chem*, 2001, **276**, 45539-45547.
6. R. Abes and J.-L. Teillaud, *Pharmaceuticals*, 2010, **3**, 146.
7. S. Krapp, Y. Mimura, R. Jefferis, R. Huber and P. Sondermann, *J Mol Biol*, 2003, **325**, 979-989.
8. K. Zheng, C. Bantog and R. Bayer, *MAbs*, 2011, **3**, 568-576.
9. Y. B. Zhang and L. Y. Chen, *Biophys Chem*, 2013, **171**, 24-30.
10. J. Shao, Y. Zhang, J. Yu, L. Guo and Y. Ding, *PLoS One*, 2011, **6**, e20342.
11. Y. Zhang, Y. Cui and L. Y. Chen, *Biophys Chem*, 2012, **160**, 69-74.
12. Y. Zhang, M. Baaden, J. Yan, J. Shao, S. Qiu, Y. Wu and Y. Ding, *J Phys Chem B*, 2010, **114**, 13839-13846.
13. E. Papaleo, P. Mereghetti, P. Fantucci, R. Grandori and L. De Gioia, *Journal of molecular graphics and modelling*, 2009, **27**, 889-899.
14. W. L. DeLano, M. H. Ultsch, A. M. de Vos and J. A. Wells, *Science*, 2000, **287**, 1279-1283.
15. E. E. Idusogie, L. G. Presta, H. Gazzano-Santoro, K. Totpal, P. Y. Wong, M. Ultsch, Y. G. Meng and M. G. Mulkerrin, *J Immunol*, 2000, **164**, 4178-4184.
16. D. Van Der Spoel, E. Lindahl, B. Hess, G. Groenhof, A. E. Mark and H. J. Berendsen, *J Comput Chem*, 2005, **26**, 1701-1718.
17. V. Hornak, R. Abel, A. Okur, B. Strockbine, A. Roitberg and C. Simmerling, *Proteins: Structure, Function, and Bioinformatics*, 2006, **65**, 712-725.
18. J. Wang, P. Cieplak and P. A. Kollman, *Journal of Computational Chemistry*, 2000, **21**, 1049-1074.
19. J. Wang, R. M. Wolf, J. W. Caldwell, P. A. Kollman and D. A. Case, *J Comput Chem*, 2004, **25**, 1157-1174.
20. J. Wang, W. Wang, P. A. Kollman and D. A. Case, *J Mol Graph Model*, 2006, **25**, 247-260.
21. A. W. Sousa da Silva and W. F. Vranken, *BMC Res Notes*, 2012, **5**, 367.
22. U. Essmann, L. Perera, M. Berkowitz, T. Darden, H. Lee and L. Pedersen, *The Journal of Chemical Physics*, 1995, **103**, 8577-8593.
23. H. J. C. Berendsen, J. P. M. Postma, W. F. v. Gunsteren, A. DiNola and J. R. Haak, *J Chem Phys*, 1984, **81**, 3684-3690.
24. W. Humphrey, A. Dalke and K. Schulten, *J Mol Graph*, 1996, **14**, 33-38, 27-38.
25. N. Guex and M. C. Peitsch, *Electrophoresis*, 1997, **18**, 2714-2723.
26. D. Qiu, P. Shenkin, F. Hollinger and C. Still, *The Journal of Physical Chemistry A*, 1997, **101**, 3005-3014.
27. V. Tsui and D. A. Case, *Journal of the American Chemical Society*, 2000, **122**, 2489-2498.
28. T. Hou, J. Wang, Y. Li and W. Wang, *J Chem Inf Model*, 2011, **51**, 69-82.
29. T. Hou, J. Wang, Y. Li and W. Wang, *J Comput Chem*, 2011, **32**, 866-877.
30. L. Xu, H. Sun, Y. Li, J. Wang and T. Hou, *J Phys Chem B*, 2013, **117**, 8408-8421.
31. H. Sun, Y. Li, S. Tian, L. Xu and T. Hou, *Phys Chem Chem Phys*, 2014, **16**, 16719-16729.
32. T. Hou, N. Li, Y. Li and W. Wang, *J Proteome Res*, 2012, **11**, 2982-2995.
33. A. Onufriev, D. Bashford and D. A. Case, *Proteins*, 2004, **55**, 383-394.
34. W. Rocchia, E. Alexov and B. Honig, *The Journal of Physical Chemistry B*, 2001, **105**, 6507-6514.
35. D. A. Case, T. A. Darden, I. T.E. Cheatham, C. L. Simmerling, J. Wang, R. E. Duke, R. Luo, R. C. Walker, W. Zhang, K. M. Merz, B. Roberts, B. Wang, S. Hayik, A. Roitberg, G. Seabra, I. Kolossvai, K. F. Wong, F. Paesani, J. Vanicek, J. Liu, X. Wu, S. R. Brozell, T. Steinbrecher, H. Gohlke, Q. Cai, X. Ye, J. Wang, M.-J. Hsieh, G. Cui, D. R. Roe, D. H. Mathews, M. G. Seetin, C. Sagui, V. Babin, T. Luchko, S. Gusarov, A. Kovalenko and P. A. Kollman, *AMBER 11*, University of California, San Francisco., 2010.
36. S. Qiu, H. Yi, J. Hu, Z. Cao, Y. Wu and W. Li, *Curr HIV Res*, 2012, **10**, 182-194.
37. F. Godschalk, S. Genheden, P. Soderhjelm and U. Ryde, *Phys Chem Chem Phys*, 2013, **15**, 7731-7739.
38. D. W. Wright, B. A. Hall, O. A. Kenway, S. Jha and P. V. Coveney, *J Chem Theory Comput*, 2014, **10**, 1228-1241.
39. D. M. van Aalten, J. B. Findlay, A. Amadei and H. J. Berendsen, *Protein Eng*, 1995, **8**, 1129-1135.
40. N. A. Baker, D. Sept, S. Joseph, M. J. Holst and J. A. McCammon, *Proc Natl Acad Sci U S A*, 2001, **98**, 10037-10041.
41. X. Wang, S. Kumar, P. M. Buck and S. K. Singh, *Proteins*, 2013, **81**, 443-460.
42. W. F. Dall'Acqua, P. A. Kiener and H. Wu, *J Biol Chem*, 2006, **281**, 23514-23524.
43. T. T. Kuo and V. G. Aveson, *MAbs*, 2011, **3**, 422-430.
44. Y. A. Yeung, M. K. Leabman, J. S. Marvin, J. Qiu, C. W. Adams, S. Lien, M. A. Starovasnik and H. B. Lowman, *J Immunol*, 2009, **182**, 7663-7671.
45. S. Siberil, C. de Romeuf, N. Bihoreau, N. Fernandez, J. L. Meterreau, A. Regenman, E. Nony, C. Gaucher, A. Glacet, S. Jorieux, P. Klein, M. P. Hogarth, W. H. Fridman, D. Bourel, R. Beliard and J. L. Teillaud, *Clin Immunol*, 2006, **118**, 170-179.
46. A. Croset, L. Delafosse, J.-P. Gaudry, C. Arod, L. Glez, C. Losberger, D. Begue, A. Krstanovic, F. Robert, F. Vilbois, L. Chevalet and B. Antonsson, *Journal of Biotechnology*, 2012, **161**, 336-348.

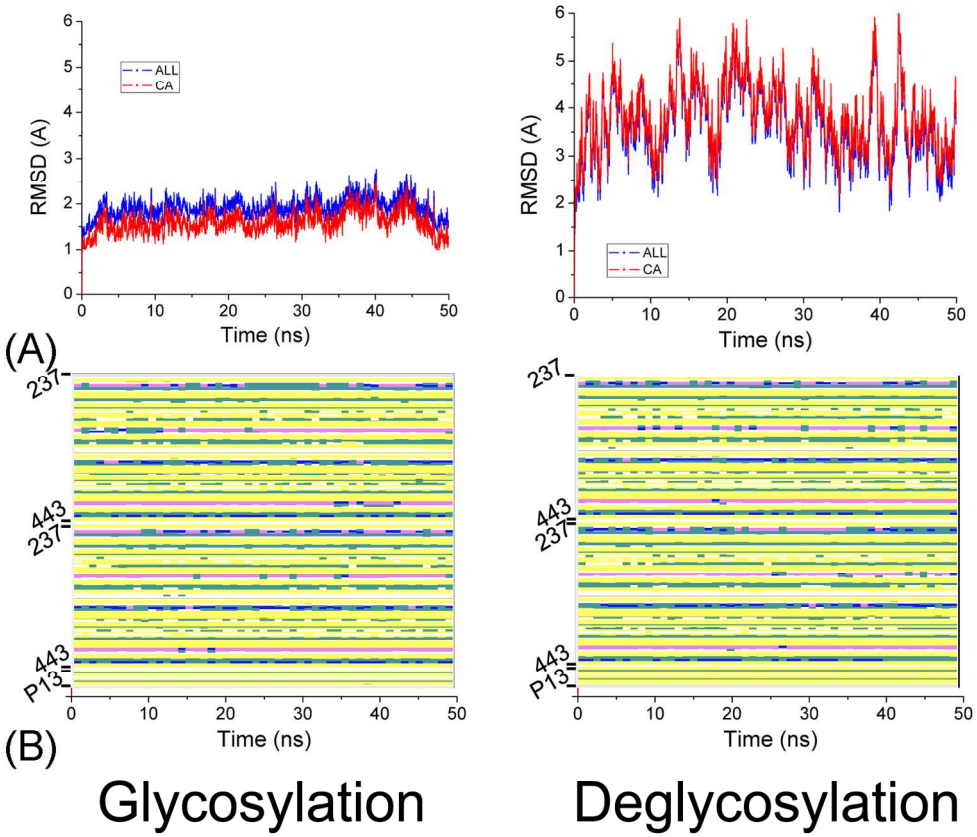

171x151mm (268 x 268 DPI)

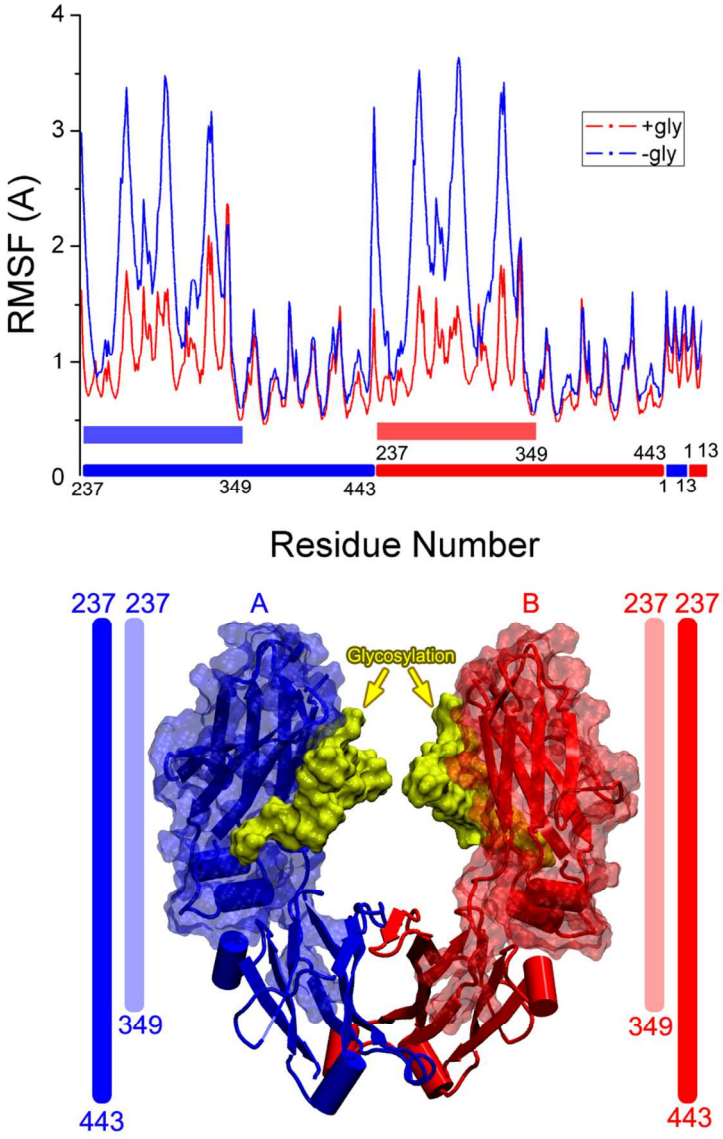

124x187mm (300 x 300 DPI)

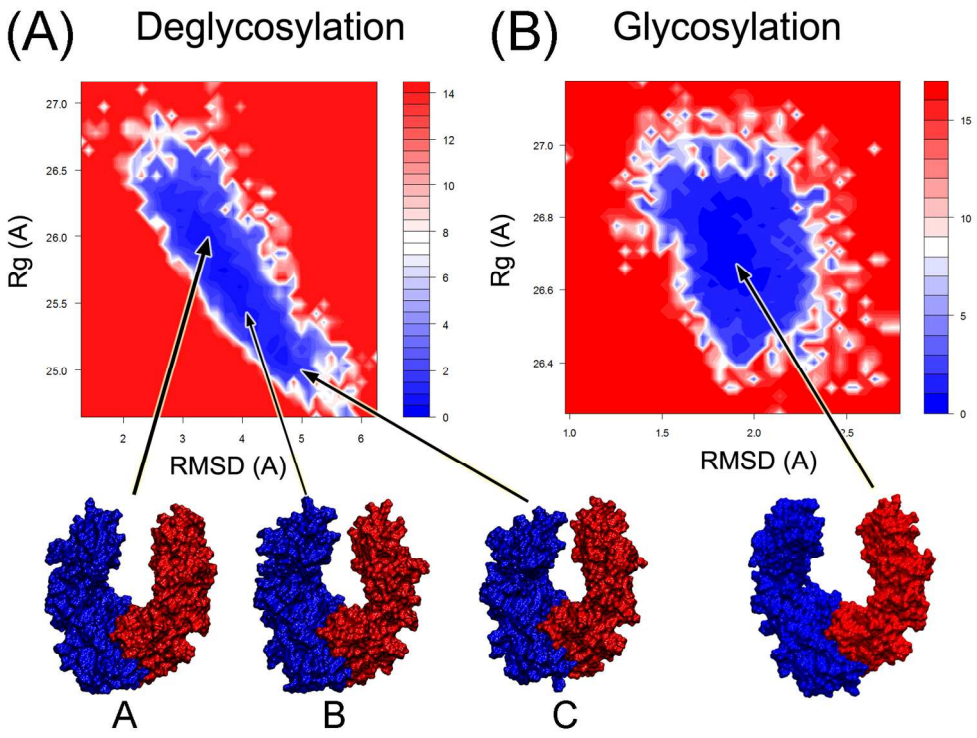

171x130mm (277 x 277 DPI)

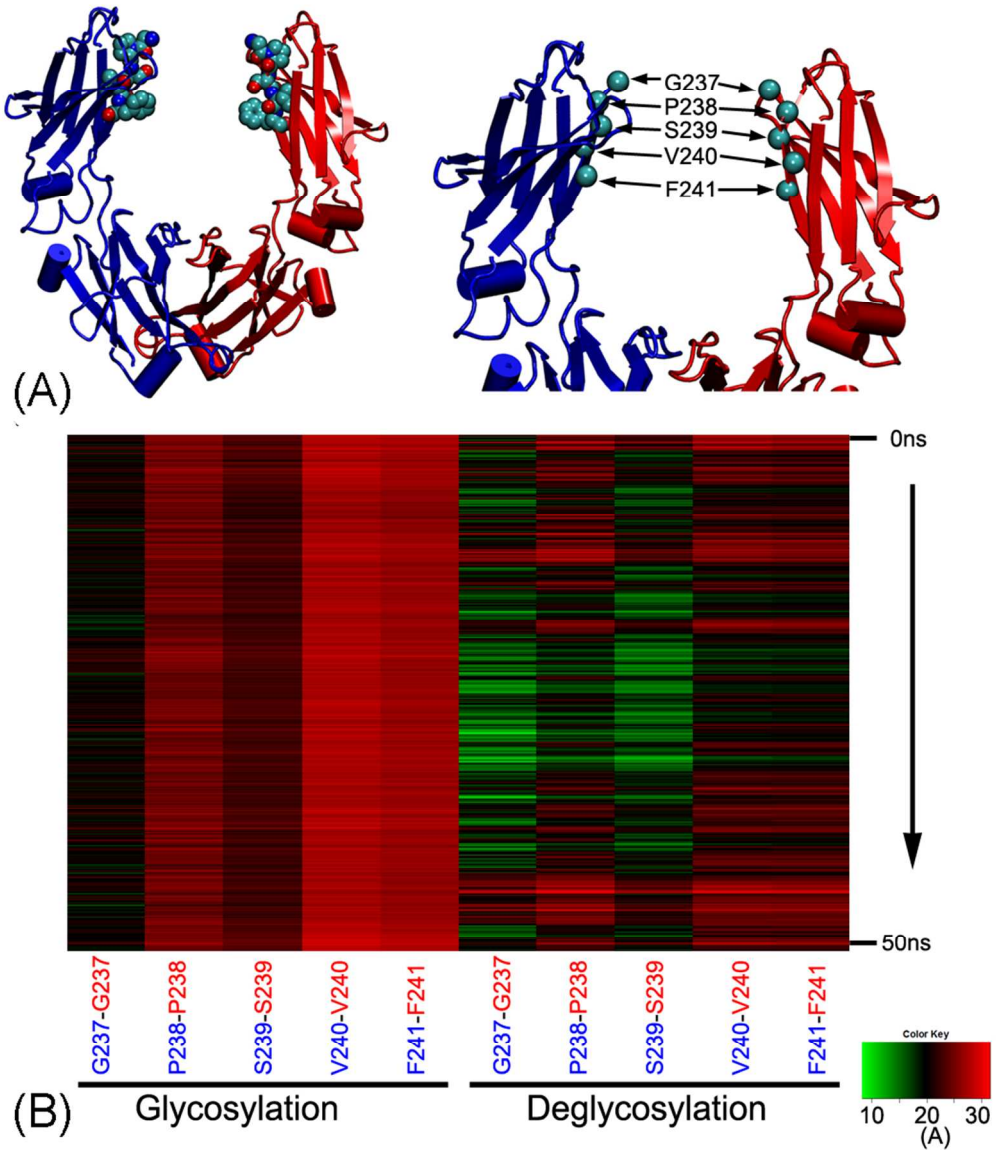

171x199mm (155 x 155 DPI)

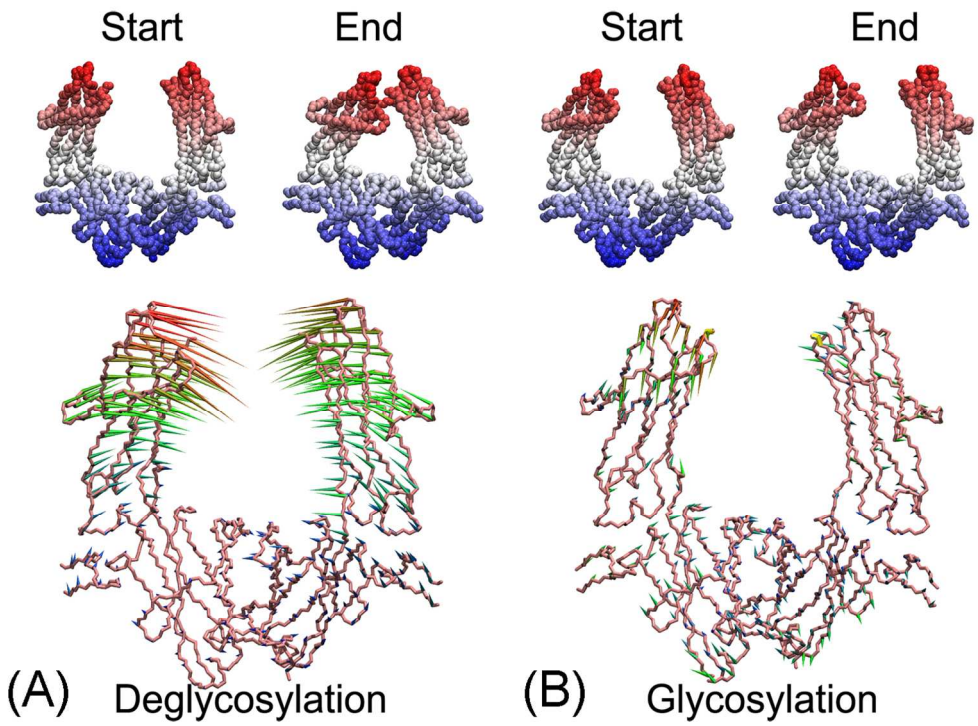

171x124mm (233 x 233 DPI)

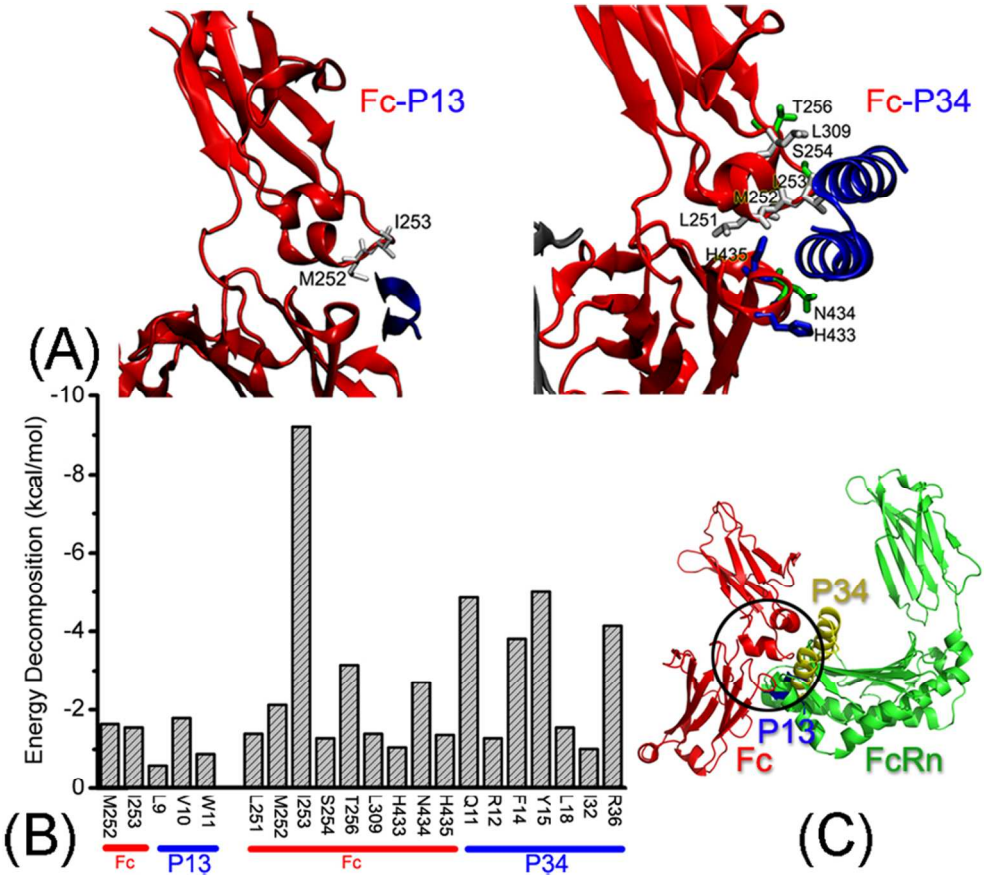

83x72mm (299 x 299 DPI)

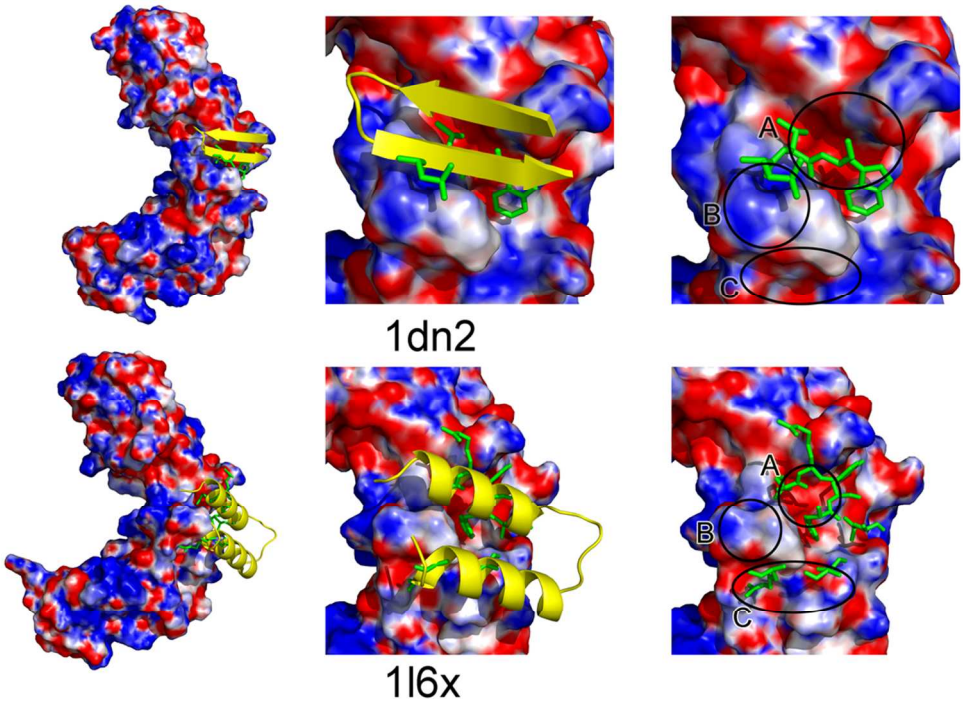

171x126mm (175 x 175 DPI)

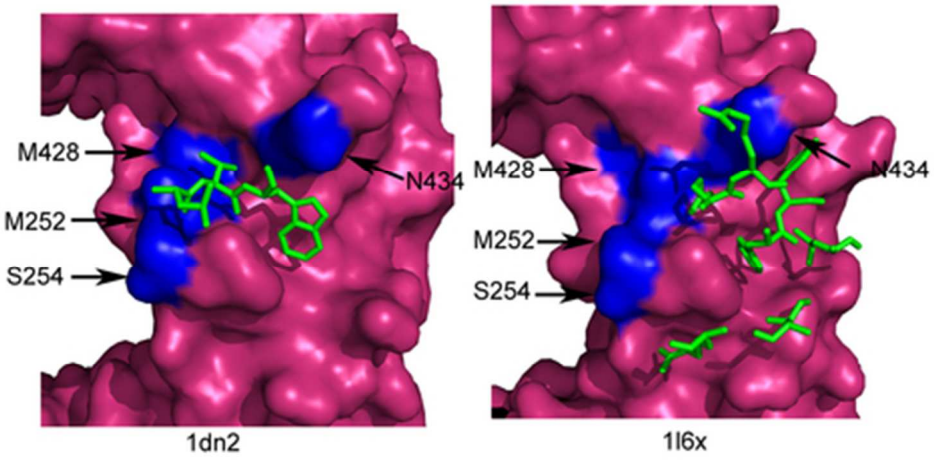

41x20mm (300 x 300 DPI)